

See discussions, stats, and author profiles for this publication at: <https://www.researchgate.net/publication/268527647>

Modeling leaf growth of rosette plants using infrared stereo image sequences

Article in *Computers and Electronics in Agriculture* · January 2015

DOI: 10.1016/j.compag.2014.10.020

CITATIONS

26

READS

209

6 authors, including:



Eren Erdal Aksoy

Halmstad University

48 PUBLICATIONS 629 CITATIONS

SEE PROFILE



Florentin Wörgötter

Georg-August-Universität Göttingen

461 PUBLICATIONS 6,433 CITATIONS

SEE PROFILE



Hanno Schar

Forschungszentrum Jülich

116 PUBLICATIONS 2,562 CITATIONS

SEE PROFILE



Andreas Fischbach

Forschungszentrum Jülich

17 PUBLICATIONS 523 CITATIONS

SEE PROFILE

Some of the authors of this publication are also working on these related projects:



Xperience [View project](#)



IntellAct [View project](#)

Modeling leaf growth of rosette plants using infrared stereo image sequences

Eren Erdal Aksoy^{*,1}, Alexey Abramov¹, Florentin Wörgötter¹, Hanno Scharr², Andreas
Fischbach², Babette Dellen³

¹*Georg-August-Universität Göttingen, BCCN, Department for Computational Neuroscience
Inst. Physics-3, Friedrich-Hund Platz 1, D-37077 Göttingen, Germany*

²*IBG-2: Plant Sciences, Forschungszentrum Jülich, 52425 Jülich, Germany*

³*Institut de Robòtica i Informàtica Industrial (CSIC-UPC)
Llorens i Artigas 4-6, 08028 Barcelona, Spain*

**Corresponding Author: eaksoy@gwdg.de*

Abstract

In this paper, we present a novel multi-level procedure for finding and tracking leaves of a rosette plant, in our case up to 3 weeks old tobacco plants, during early growth from infrared-image sequences. This allows measuring important plant parameters, e.g. leaf growth rates, in an automatic and non-invasive manner. The procedure consists of three main stages: preprocessing, leaf segmentation, and leaf tracking. Leaf-shape models are applied to improve leaf segmentation, and further used for measuring leaf sizes and handling occlusions. Leaves typically grow radially away from the stem, a property that is exploited in our method, reducing the dimensionality of the tracking task. We successfully tested the method on infrared image sequences showing the growth of tobacco-plant seedlings up to an age of about 30 days, which allows measuring relevant plant growth parameters such as leaf growth rate. By robustly fitting a suitably modified autocatalytic growth model to all growth curves from plants under the same treatment, average plant

growth models could be derived. Future applications of the method include plant-growth monitoring for optimizing plant production in green houses or plant phenotyping for plant research.

12 *Keywords:* leaf segmentation, leaf tracking, leaf modeling, plant growth, phenotyping

13 **1. Introduction**

14 With increasing requirements for food due to a growing world population, optimizing
15 plant production is becoming an important factor for the agricultural industry. Plant per-
16 formance and productivity results from a complex interaction between its genotype and
17 environment, resulting in its expressed properties, i.e. its phenotype. Thus, if one seeks
18 to understand these interdependencies, e.g. to achieve larger yields, plant phenotypes in
19 terms of expressed plant structure and function need to be analyzed quantitatively. For
20 this task automatic, non-invasive methods are highly desirable, but problems arise from
21 the complex and varying appearance of plants, making it difficult to detect and recognize
22 relevant plant organs and growth patterns.

23 Previously both color and stereo vision have been used to obtain some relevant plant
24 features, mainly for recognition and classification purposes (Loch et al., 2005; Moeslund
25 et al., 2005; Quan et al., 2006; Biskup et al., 2007; Song et al., 2007; Jin and Tang, 2009;
26 Alenyà et al., 2011a; Teng et al., 2011; Silva et al., 2013; Wang et al., 2013), but those
27 procedures are error prone, or require the concurrence of a user to correctly segment and
28 characterize individual leaves. For instance, Quan et al. (2006) modeled plants directly
29 from a set of images for a better supervised leaf segmentation. Jin and Tang (2009) de-
30 tected corn plants by only using depth images without dealing with the tracking issue. Leaf
31 tracking has, to our knowledge, so far only been performed with unambiguously identified

32 leaves. For example, Biskup et al. (2007) tracked the leaf orientation angles, and Polder
33 et al. (2007) used penalized likelihood warping and robust point matching of leaf contours
34 in order to detect emerging damages caused by disease. Alenyà et al. (2011b) showed how
35 a robot arm can track a manually selected single leaf using some geometrical characteris-
36 tics and color information. The problem of tracking multiple leaves was not addressed by
37 these works. The work in (De Vylder et al., 2013) uses active contours to track multiple
38 leaves, but they process time lapse plant images in batch once the complete sequence is
39 acquired. Their proposed segmentation approach is triggered with the last frame of the
40 sequence in a semi-supervised manner and the detection phase can omit new leaves since
41 it goes to the first frame starting from the last one. De Vylder et al. (2011) combined
42 active contours with a Bayesian framework to eliminate parameter tuning steps in the seg-
43 mentation and tracking phases. However, they need manually segmented images to have
44 a good estimate of the probability distribution functions for the calculation of internal and
45 external probabilities. Both approaches (De Vylder et al., 2013, 2011) have also not been
46 tested on plant sequences that last longer than 3 days.

47 Along this line, the European project GARNICS (Gardening with a Cognitive System)¹
48 aimed at 3D sensing of plant growth and building perceptual representations for learning
49 the links to actions of a robot gardener (see Figure 1). The project encompassed both
50 the long-term learning of treatments to achieve specific goals (maximum leaf growth, ho-
51 mogeneous plant growth) as well as the short-term robot interaction with plants (for leaf
52 surface measurement, disocclusion, probing), and this study has been conducted in this
53 context.

¹<http://www.garnics.eu>



Figure 1: Robot gardener used in the European project GARNICS. A black-and-white 5 MP camera with infrared filter and required illumination devices were mounted on a lightweight KUKA LBR4 robot arm. For each tobacco plant the robot arm captured a stereo image pair from a top view at every hour.

54 More precisely, we address the problem of sensing and controlling plant growth pa-
55 rameters by ways of leaf tracking and model fitting, using a stereo infrared camera set-up,
56 monitoring tobacco seedlings during their first three weeks of growth. A major difficulty
57 hereby arises from the complex appearance of plants in the image. Leaves are weakly
58 textured, often overlapping, thus occluding each other, and their form may be distorted in
59 the 2D projection due to steep leaf angles with respect to the camera view. Under these
60 conditions, the automated image segmentation of individual leaves is highly challenging,
61 and cannot be guaranteed. In this work, we first over-segment the infrared images and then
62 employ a merging procedure using a 2D leaf-shape model, but also incorporating 3D in-
63 formation from stereo matching. The main growth curves of the plant leaves are extracted
64 and used to analyze plant development over time. Segmentation failures appear as noise
65 in the system, and can be handled at least to some degree. Once the main growth curves

66 corresponding to the individual leaves of the plant are found, erroneous segments can be
67 removed, and by using a leaf-shape model, the growth rates for each identified leaf can be
68 computed.

69 Rosette plants are commonly used in plant research facilities, and the automatic growth
70 analysis of seedlings would come in handy for many laboratories. Furthermore, growth
71 monitoring of seedlings can be used in plant production to optimize plant treatments, e.g.
72 with respect to the provision of water and nutrients or light requirements. Size and color
73 distribution of plant leaves over time are important cues to monitor the lack of such re-
74 quirements, avoiding plant stress situations.

75 Note that this study has also been described as a part of a patent (Wörgötter et al.,
76 2013).

77 **2. Plant Material**

78 Six tobacco plants (*Nicotiana tabacum* cv. *Samsun*) were grown under constant light
79 conditions ($500\mu\text{E m}^{-2}\text{s}^{-1}$) with a 16h/8h day/night rhythm. Three of them (Plant IDs
80 79329, 79335, and 79338) received 1.8ml of water every other hour (“Treatment 1”), the
81 others (Plant IDs 79330, 79336, and 79339) received 0.9ml of water and 0.5ml of nutrient
82 solution with 1% Hakaphos green every other hour (“Treatment 2”). Water and nutrient
83 solution were applied by the GARNICS robot system, positioning small tubes, one for wa-
84 ter and one for nutrient solution, at predefined locations and pumping using an automated
85 flexible-tube pump.

86 In the GARNICS project, treatments were selected to produce training data for a cog-
87 nitive system. The actual amounts of water and nutrient solution are therefore well adapted

88 to the soil substrate such that the sets of plants show distinguishable performance of gen-
89 erally well growing plants. Finding an optimal treatment was left for the system. The soil
90 used for the experiment (“Kakteenerde”) has low nutrient content and dries relatively fast
91 with an approximately exponential behavior $A = A_0 \exp(-t/\tau)$, where $\tau \approx .7$ days.

92 We applied the proposed leaf tracking and modeling algorithm to tobacco-plant se-
93 quences showing the growth from germination well into the leaf development stage, i.e.
94 we started our observations at growth stage 09 and typically stopped at stage 1006 (accord-
95 ing to the extended BBCH-scale presented in CORESTA (2009)), due to size restrictions.

96 **3. Method**

97 *3.1. Overview*

98 Our framework for continuous measurement of plant growth parameters consists of
99 three main parts: data acquisition and preprocessing, segmentation of all frames from a
100 plant video sequence, and consistent leaf tracking and modeling of the segmented leaves.
101 A schematic showing all steps of the procedure and labeled by numbers is presented in
102 Figure 2.

103 As input data we use gray-scale stereo images acquired with an infrared camera at-
104 tached on a robot arm. We compared different illumination options and found that plant
105 structures and boundaries between tobacco leaves could be detected more easily for in-
106 frared light than for visible light. In addition, plants do not react to the applied 880nm
107 IR light, e.g. by photosynthetic activity. Consequently, illumination and acquiring images
108 at night is possible without influencing plant growth, in contrast to visible light. A pair
109 of images (left and right) is captured at each time step by moving the robot head with the

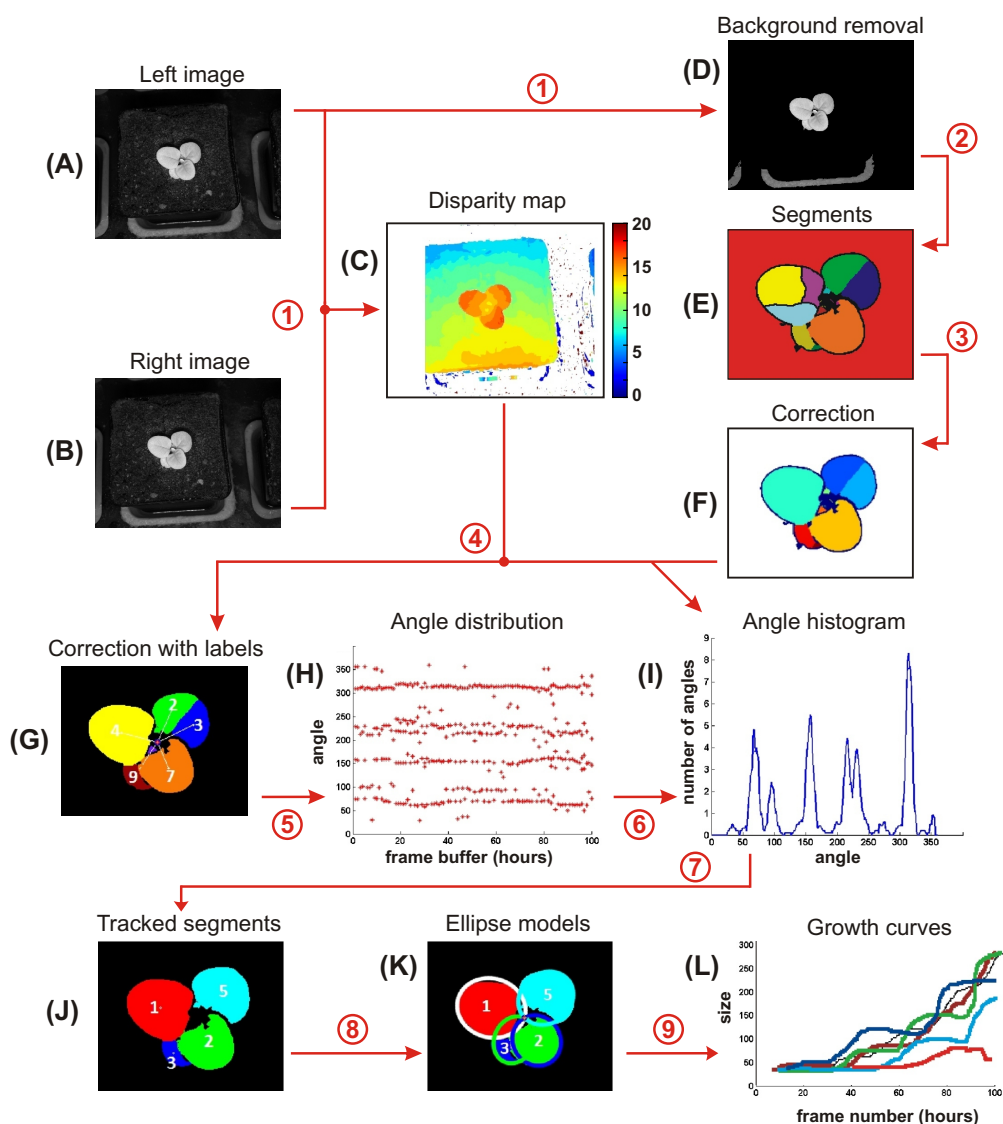


Figure 2: Schematic of the multi-level procedure for segmenting and tracking leaves. Numbers mark the different computational steps of the procedure. (A) Acquired left frame. (B) Acquired right frame. (C) Disparity map estimated using block matching. (D) Left frame after background removal. (E) Image segmentation results using the method of superparamagnetic clustering of data (here and further scaled up for a better visibility). (F) Segments after segment merging, and (G) after relabeling. (H) Angle distribution of corrected segments for 100 frames. (I) Angle histogram derived from the angular distribution. (J) Tracked segments with reassigned unique labels. (K) Ellipse models fitted to the tracked segments. (L) Plant growth curves estimated from ellipse models.

110 infrared camera and light source, providing a stereo baseline (see Figure 2(A) and (B)).
111 In step 1 of the procedure, we compute a depth (disparity) map from the stereo pair using
112 a block-matching algorithm from the OpenCV library Bradski (2000) (see Figure 2(C)).
113 This method gave preferable results compared to other methods. We further removed the
114 background from the scene to simplify the following computations (see Figure 2(D)).

115 Next, in step 2, each preprocessed infrared image of the sequence is segmented in-
116 dependently. Afterwards, each leaf is represented by one or more segments as shown in
117 Figure 2(E). In step 3, we employ a merging procedure to group the segments into leaf
118 shapes (Figure 2(F)) by finding the partition that minimizes the overlap between the con-
119 vex hulls of the segments. This is a good enough working assumption as long as the
120 leaves have convex shapes. This merging stage is a necessary improvement, but it still
121 does not guarantee success. Sometimes there are over-segmentations which remain unre-
122 solved, as shown in Figure 2(F). Note that after merging, the segments are relabeled (see
123 Figure 2(G)).

124 In step 5 of the procedure, the position of the centroid of each segment is computed
125 with respect to the plant stem position in polar coordinates. The plant stem can be found
126 with sufficient accuracy by computing the centroid of the foreground (containing only the
127 plant) at an early growth stage. By presenting each segment as a data point in an angle-
128 time plot, growth tracks can be made visible because the tobacco-plant leaves do hardly
129 change their azimuthal angle (Figure 2(H)). Leaves that are growing in the same direction
130 can be distinguished based on their depth values. Hence, when computing the angular
131 histogram of the centroids over a larger time interval (step 6 of the procedure), the data
132 points of the growth tracks accumulate at the angular positions of the corresponding leaves

133 (see Figure 2(I)). By first detecting the peaks in the histogram using a threshold, we can
134 cluster the segments belonging to the different tracks and assign them unique, temporally
135 consistent labels in step 4 (see Figure 2(J)). In the final step (9), tracked segments, corre-
136 sponding to leaves, are used for fitting appropriate ellipse models (see Figure 2(K)) and
137 estimating growth curves for individual leaves as shown in Figure 2(L).

138 *3.2. Image Acquisition*

139 For image acquisition a black-and-white 5 MP camera with infrared pass filter has
140 been used. Images have been taken at regular, hourly time intervals for each plant over a
141 time period of 30 days. The camera was mounted on a lightweight KUKA LBR4 robot
142 arm (see Figure 1). For each plant the robot arm captured a stereo image pair from a top
143 view every hour by moving a certain distance (app. 5 mm) along the baseline.

144 *3.3. Preprocessing*

145 Before segmenting the images, we remove the background as shown in the second
146 row of Figure 3. The table, the plant pot, and the soil visible in the near infrared (NIR)
147 images can be easily eliminated by applying a threshold. Furthermore, a disparity map is
148 computed with a standard block-matching technique from the stereo infrared images.

149 *3.4. Leaf Segmentation*

150 For segmenting the images, we use the method of superparamagnetic clustering of data
151 which runs in real-time on a Graphics Processing Unit (GPU). The method of superpara-
152 magnetic clustering is inspired by systems of interacting ferromagnets or spins. These
153 systems are characterized by three phases. At low temperatures, spins are fully aligned
154 with one another, while at intermediate temperatures, groups of aligned spins coexists. At

155 higher temperatures, the order breaks down into a disordered state. When representing
156 pixels by spins and defining spin-spin interactions dependent on the similarity of adja-
157 cent pixels, a natural partition of the image can be found in the superparamagnetic regime
158 simulating the stochastic dynamics of the system with a Metropolis algorithm.

159 The method of superparamagnetic clustering has been described in detail elsewhere
160 Abramov et al. (2012). Superparamagnetic clustering has been used previously to segment
161 leaves based on color and depth acquired with a Kinect camera (Wallenberg et al. (2011)).
162 However, in this case, plants were fully grown and leaves considerably larger. In our
163 experimental set-up, leaves are smaller, and the task of obtaining sufficiently accurate
164 depth information for depth-based segmentation would be far more challenging. Typical
165 segmentation results obtained by this technique are shown in the last row of Figure 3.

166 Due to varying light conditions and very low intensity differences at the leaf borders,

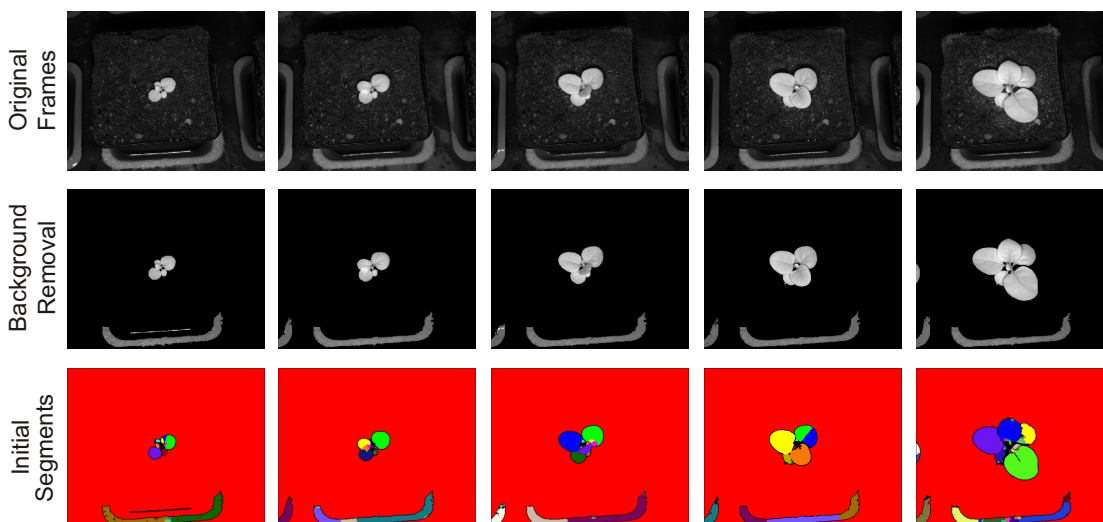


Figure 3: Segmentation of near infrared (NIR) images using the method of superparamagnetic clustering. First row shows left input frames captured with an infrared camera, middle row indicates frames after the background removal, and the last row shows initial segmentation results (after step 2 of the procedure).

167 leaves may be wrongly merged by the method. To avoid this, the segmentation runs in the
168 over-segmentation mode (see Figure 3). This strategy ensures that segments adhere better
169 to leaf borders. Leaves represented by more than one segment can be recovered later on
170 (see Section 3.5), while recovery of two (or more) leaves from one big wrongly merged
171 segment (under-segmentation) is more difficult.

172 3.5. *Segment merging*

173 The output given by the image segmentation module many times splits one leaf into
174 more than one segment and may contain noisy regions, such as a part of the pot or some
175 areas of high intensity compared to the background. Therefore, additional procedures are
176 required in order to obtain a better segmentation. The first major improvement is achieved
177 by correcting the initial segments with a leaf-shape descriptor. For this purpose tobacco
178 plant leaves can be described by their convex hulls with sufficient accuracy.

179 The segment-merging procedure works as follows. First of all, segments with cen-
180 troids located far from the plant stem are eliminated (see the first row in Figure 4). Noisy
181 speckles are removed as well (see the second row in Figure 4). Then a graph is built where
182 the centroids of the segments represent the graph nodes. Edges are drawn between two
183 nodes if the segments are smaller than a threshold apart both in (x, y) distance and depth.
184 Each edge represents a possible merge. Hence, for a total number of s edges, there are
185 2^s possible merging configurations M_i . Neglecting occlusions, the desired segmentation
186 should more or less preserve the shape of the leaves, i.e., using the segment's convex hull
187 as leaf-shape model, the total overlap of the convex hulls of all segments should be smallest
188 for this configuration. Let now be C_j the convex hull of segment j , then we compute the
189 overlap of a particular merging configuration M_i as $O_i = \sum_{e_{lm} \in M_i} C_l \cap C_m + \sum_k C_k \cap B$,

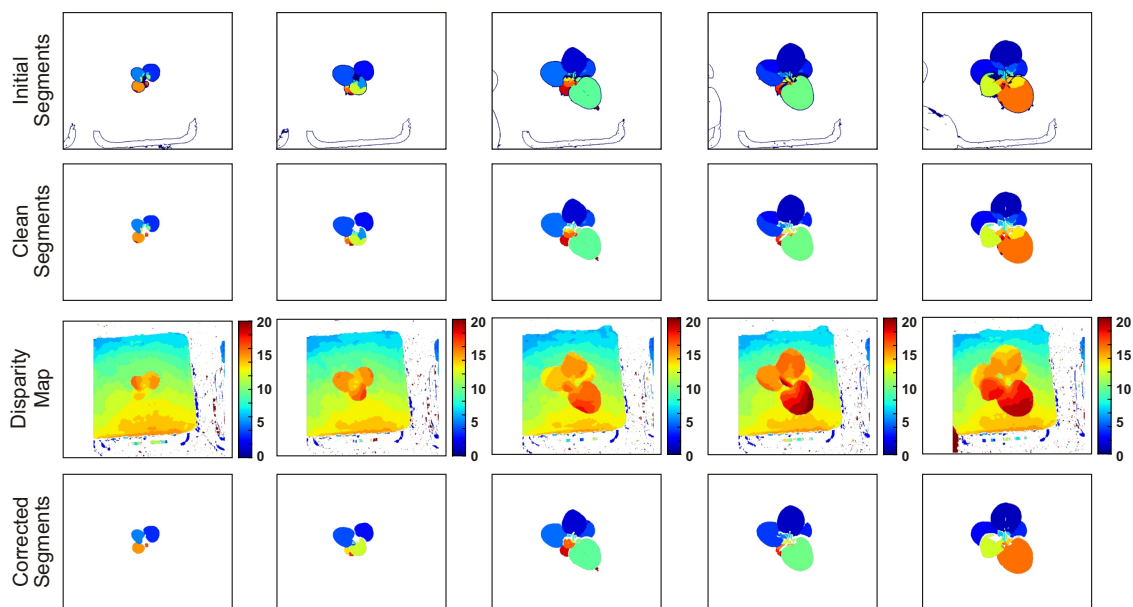


Figure 4: Segment correction performed by the convex hull approximation with depth information. Top row shows initial segments. Second row indicates clean input segments without noise and borders. Third row represents disparity maps estimated by the block matching technique for a pair of NIR images. Final segments after segment merging are shown in the last row (after step 3 of the procedure).

190 where B is the background region. We select the merging configuration with the smallest
 191 overlap. For a small number of edges, we can simply evaluate all possible configurations.
 192 This is the case in our scenario. For large number of edges, approximate methods would
 193 have to be employed to find the minimum.

194 The depth data (see the third row in Figure 4) is used to remove edges between neigh-
 195 boring segments that have a large difference in disparity. This also helps to keep s reason-
 196 ably small. Typical results of the segment-merging procedure segmentation are shown in
 197 the last row of Figure 4.

198 Merging segments that represent a leaf based on shape features is a difficult problem
 199 for the following reasons: Only a small part of the boundary of a leaf segment corresponds

200 to the actual leaf boundary (the other ones are inner boundaries, i.e, non-leaf boundaries).
 201 Pairwise merging, as employed in standard split-and-merge approaches, will thus only be
 202 successful for simple cases because the shape of the whole leaf will only become apparent
 203 when all the segments have been merged correctly and all inner boundaries have been
 204 removed through the merging process. This is a typical chicken-egg problem. Occlusion
 205 adds further difficulties by altering the visible shape of the leaves. For this reason, given
 206 the small number of segments, we opted for the described merging technique which avoids
 207 having to apply a standard pairwise merging procedure (Horowitz and Pavlidis (1974);
 208 Aleny \tilde{A} et al. (2013)) and instead tests for all possible combinatorial solutions.

209 3.6. Tracking

210 Usually leaves grow at an almost constant azimuth angle with respect to the plant stem
 211 during their development, and even if two leaves have the same angle, their depth values
 212 typically are different. Therefore, we can make use of the natural growth pattern of plant
 213 leaves for solving the tracking issue.

214 For each frame, we first calculate coordinates of the plant stem $p = \{p_x, p_y\}$ as

$$p_x = \frac{1}{N} \sum_{i=1}^N s_{x_i} \quad , \quad p_y = \frac{1}{N} \sum_{i=1}^N s_{y_i} \quad , \quad (1)$$

215 where N is the total number of existing segments, whose centers are given by $\{s_x, s_y\}$.

216 Each segment center is then represented by r and θ defining the radius and angle in
 217 polar coordinates as

$$r = \sqrt{(s_x - p_x)^2 + (s_y - p_y)^2} \quad , \quad \theta = \arctan 2\left(\frac{s_y - p_y}{s_x - p_x}\right) \quad . \quad (2)$$

218 At each acquired frame, all extracted N segment angles are combined into a histogram
 219 H representing the distribution of angles over previous T frames as

$$H = \{h_i : i \in [1, 2, \dots, \frac{360}{k}]\},$$

$$h_i = \sum_{n=1}^N \sum_{t=1}^T \delta_{n,t} \quad , \quad (3)$$

$$\delta_{n,t} = \begin{cases} 1 & \text{if } i - 1 < \frac{\theta_{n,t}}{k} < i \\ 0 & \text{else} \end{cases} \quad , \quad (4)$$

220 where k is the bin size. In our experiments k and T values are chosen as 10 and 100
 221 unless otherwise stated. Fig. 5 (top row) shows four plant images. The corresponding
 222 segments from the merging procedure are shown in the second row. The respective angular
 223 distributions of their centroid positions over 100 frames are plotted in the third row of
 224 Fig. 5. The resulting histogram representation for each plant image is depicted in the
 225 fourth row in Fig. 5.

226 We further continue with calculating local maxima (i.e. peaks) in each histogram and
 227 use them to cluster the data. Let m_i and m_j be the angle positions of two local maxima
 228 derived from a given angle distribution. The maximum at m_j is basically ignored if $m_i -$
 229 $m_j < \tau_d$, where τ_d is a threshold. In our experiments, we use $\tau_d = 40^\circ$. The extracted local
 230 maxima (i.e. all m_i) are shown as red circles in Fig. 5. All other local maxima (i.e. all m_j)

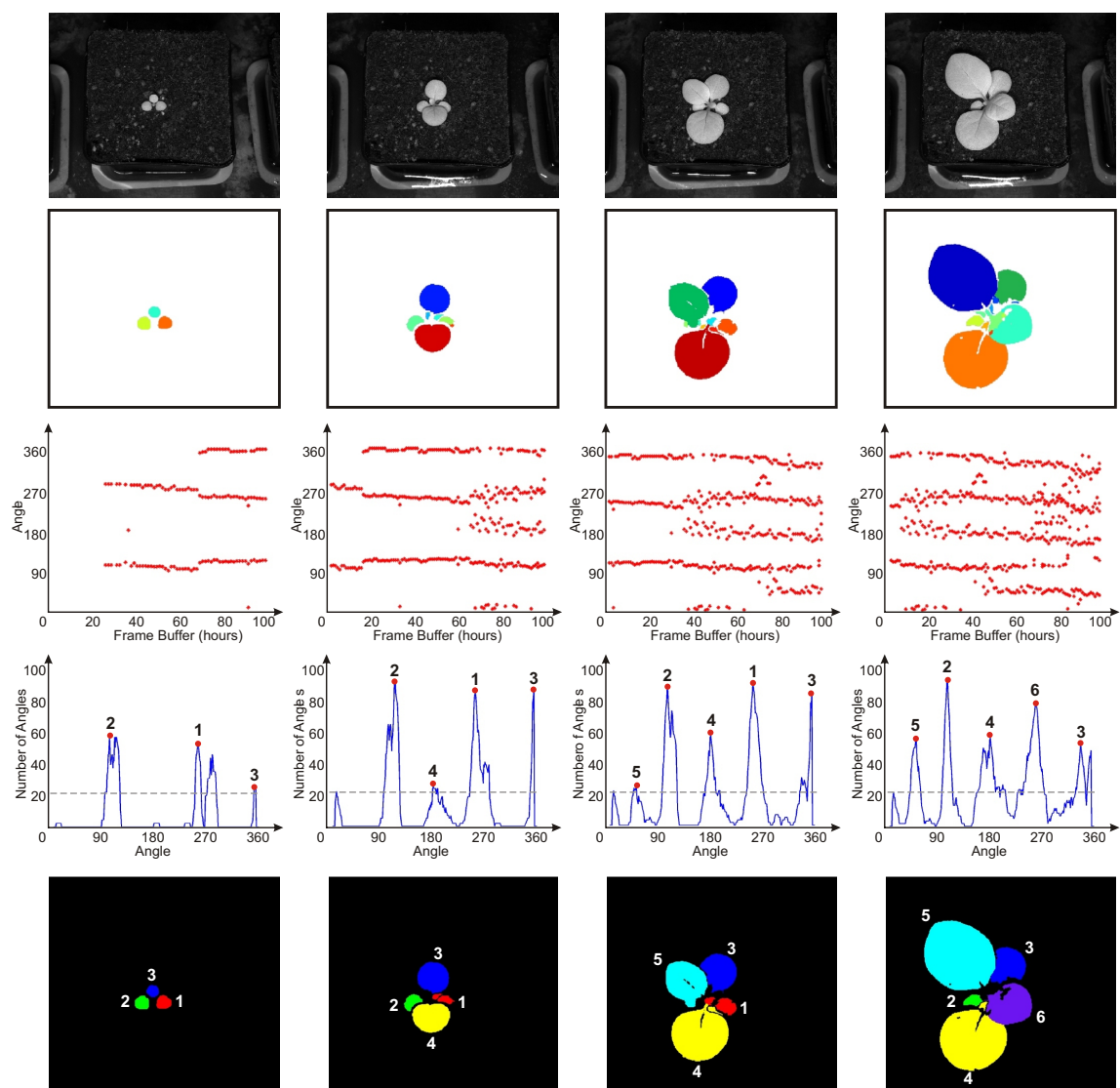


Figure 5: Tracking plant leaves with segment angles. Top row shows sample original plant images with corresponding corrected segments depicted in the second row. Segments are here scaled up for a better visibility. Respective angular distribution of segments over 100 previous frames are illustrated in the third row. Histogram representation of each distribution is depicted in the fourth row. Circles in red indicate calculated final local maxima with assigned unique labels. Dashed lines show the threshold values for local maxima. Last row indicates the final tracked leaf segment labels with their unique labels.

231 are ignored since their distances to their nearest neighbors are below threshold. We also
 232 ignore those maxima which are smaller than the average histogram value

$$\tau_m = \frac{k}{360} \sum_{i=1}^{\frac{360}{k}} h_i \quad . \quad (5)$$

233 The threshold value τ_m for each histogram is shown as dashed lines in the fourth row of
 234 Fig. 5.

235 The tracking phase is concluded by reassigning a new unique label l_i for each maxima
 236 m_i^f at frame number f . The label l_i is transferred to another local maximum m_j^{f+1} in the
 237 next frame $f + 1$, if those maxima are neighbors within a certain threshold τ_d such that
 238 $|m_i^f - m_j^{f+1}| < \tau_d$. In this way, the final label-maxima correspondence map is updated
 239 at each frame to track segments continuously. In Fig. 5 (fourth row) the assigned labels
 240 corresponding to the extracted local maxima (indicated by red circles) are displayed. The
 241 first image shows the plant with three leaves, i.e. the cotyledons and first true leaf, then
 242 three more leaves appear one after the other.

243 During the tracking phase, the disparity values of corrected segments are used to dis-
 244 tinguish leaves overlapping one another as shown in the last column of Fig. 5. Here, a
 245 new leaf, assigned with label 6, is appearing and occluding the leaf with number 1. In this
 246 case, these two leaves have almost the same angle, however, due to the differences in their
 247 disparity values, a new label can be assigned to the leaf. The final segmentation result is
 248 shown in the last row of Fig. 5.

249 *3.7. Leaf modeling and extracting leaf-growth curves*

250 Since leaves can occlude each other, the size of the tracked segments extracted using
 251 the methods described in the previous section cannot be used directly to estimate plant
 252 growth parameters. To address weak to medium occlusions we fit an ellipse model defined
 253 as $\xi = \{\mathcal{C}, \Theta, \mathcal{H}, \mathcal{W}\}$, where \mathcal{C} , Θ , \mathcal{H} , and \mathcal{W} represent ellipse center position, tilt angle,
 254 and the lengths of the major and minor semiaxes (height and width), respectively, to each
 255 tracked segment.

256 In order to calculate these ellipse parameters, we first determine each leaf tip position
 257 \mathcal{T} , i.e., a segment point with the maximum distance to the plant stem, from N segment
 258 edge points (e_x, e_y) as

$$\mathcal{T} = \{\mathcal{T}_x, \mathcal{T}_y\} = \arg \max_i (d_i) \quad ,$$

$$d_i = \sqrt{(e_{x_i} - p_x)^2 + (e_{y_i} - p_y)^2} \quad , \quad i \in [1, \dots, N] \quad , \quad (6)$$

259 where p_x and p_y are the plant stem coordinates given in Eq. (1). We can now calculate
 260 the ellipse centroid coordinates $\mathcal{C} = \{\mathcal{C}_x, \mathcal{C}_y\}$ as,

$$\mathcal{C}_x = \frac{\mathcal{T}_x + p_x}{2} \quad , \quad \mathcal{C}_y = \frac{\mathcal{T}_y + p_y}{2} \quad . \quad (7)$$

261 Next, Θ , \mathcal{H} , and \mathcal{W} parameters can be approximated as

$$\Theta = \arctan 2\left(\frac{\overline{T}_y - p_y}{\overline{T}_x - p_x}\right), \mathcal{H} = \frac{\sqrt{(\overline{T}_x - p_x)^2 + (\overline{T}_y - p_y)^2}}{2}, \mathcal{W} = \frac{1}{N} \sum_{i=1}^N d_i, \quad (8)$$

262 where d is the distance of N segment edge points to the plant stem and is given in Eq. (6).

263 Leaf area is then computed from the respective ellipse size depending on \mathcal{H} and \mathcal{W} values.

264 Fig. 6 shows an example how segments are corrected, labels tracked, and ellipses
 265 fitted. In the top row, individual segmentations after segment merging (step 3) of the
 266 method are presented. The second row shows segments with reassigned labels after the
 267 tracking process has been completed (steps 5-7). The last row shows the ellipse mod-
 268 els fitted to each segment. A movie with derived segments and ellipse models can be
 269 found at www.dpi.physik.uni-goettingen.de/~eaksoye/GARNICS. Fig-

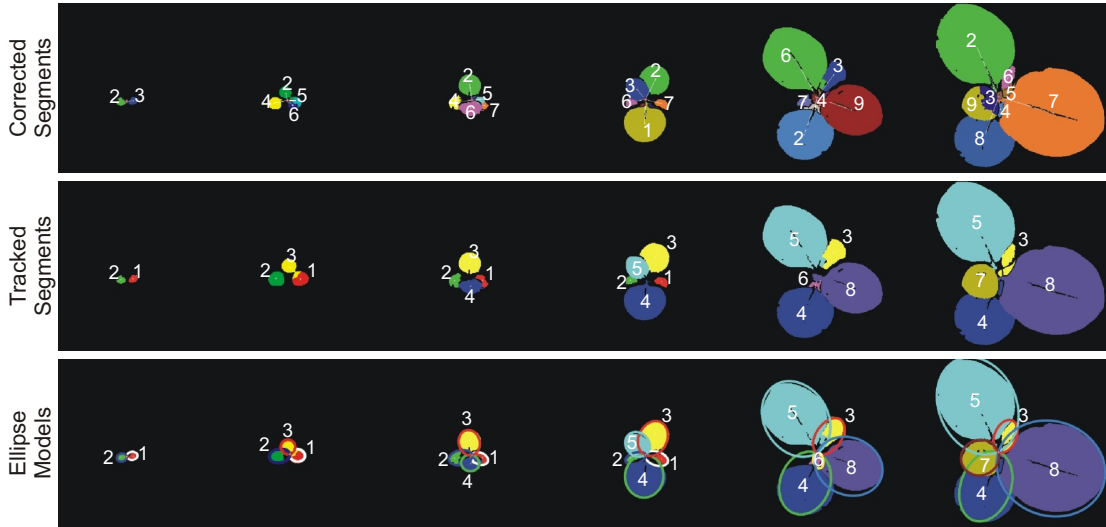


Figure 6: Leaf modeling with ellipses. Top row shows sample frames with corrected segments. Second row depicts corresponding tracked segments with reassigned unique labels. Here, each segment color represents one unique label. Last row is with final ellipse models estimated for each tracked leaf.

270 ure 7 shows ellipse tracking results for all six plants.

271 Our leaf modeling approach is a searching-based method and there exist similar works
272 in the literature (Song and Wang, 2007; Kaewapichai and Kaewtrakulpong, 2008). Chien
273 et al. (2011) proposed an alternative ellipse detection framework which applies elliptical
274 Hough transform to different levels in the image pyramid. Although this approach is robust

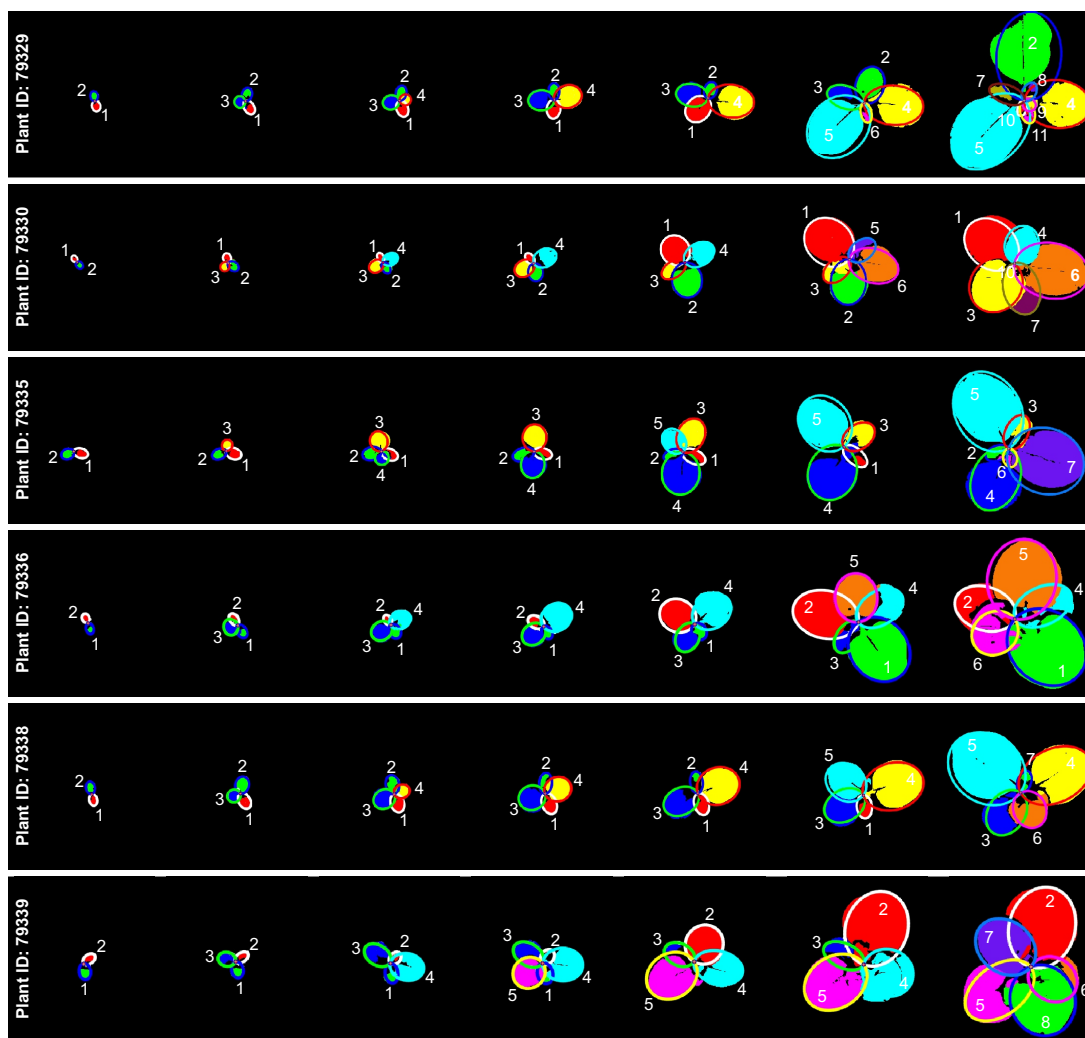


Figure 7: Tracking results and estimated ellipse models for six different tobacco plants.

275 to noise during the extraction of multiple ellipses, it cannot be applied to our plant image
276 sequences since small leaf segments, observed in the first weeks of the seedling, can vanish
277 in the coarsest resolution in the image pyramid. Thus, detection of leaves can be delayed
278 in the temporal scale.

279 3.8. *Resolving total occlusion*

280 In some cases, we observed that disparity and angle cues from Section 3.6 are not
281 enough to distinguish between leaves. When a leaf is completely occluded by a subse-
282 quently appearing leaf, the first leaf's growth curve is sometimes continued by the second
283 leaf. See e.g. Figure 7 Plant ID: 79330: Cotyledons (segments 1 and 2 in red and green,
284 respectively) grow to a small size as expected, but in the 5th and following depicted time
285 instances seem to grow strongly. Same is true e.g. for Plant ID 79336. Fortunately this can
286 be easily detected and corrected when plotting growth curves in terms of ellipse sizes as a
287 function of time (cmp. log-plots of the growth curves in Figure 8).

288 The raw data (Figure 8 top left) is median filtered with a filter length of 24h in order
289 to suppress diurnal variations. Subsequently it is smoothed and small gaps interpolated by
290 normalized convolution Knutsson and Westin (1993) using a Gaussian kernel with stan-
291 dard deviation 9h, length 27h (Figure 8 top right). The resulting smooth curves are filtered
292 to be monotonically increasing by processing them in positive time direction, keeping a
293 vale if its is the current maximum, else replacing the current value by the so far seen max-
294 imum (Figure 8 bottom left). This enforces the assumption that leaves are not shrinking.
295 These smooth monotonic curves are then cut into separate curves at gaps (cmp. Figure 8
296 bottom left, black lines, with the corresponding lines in Figure 8 bottom right), or when
297 an almost non-growing part is followed by a strongly growing one (cmp. Figure 8 bottom

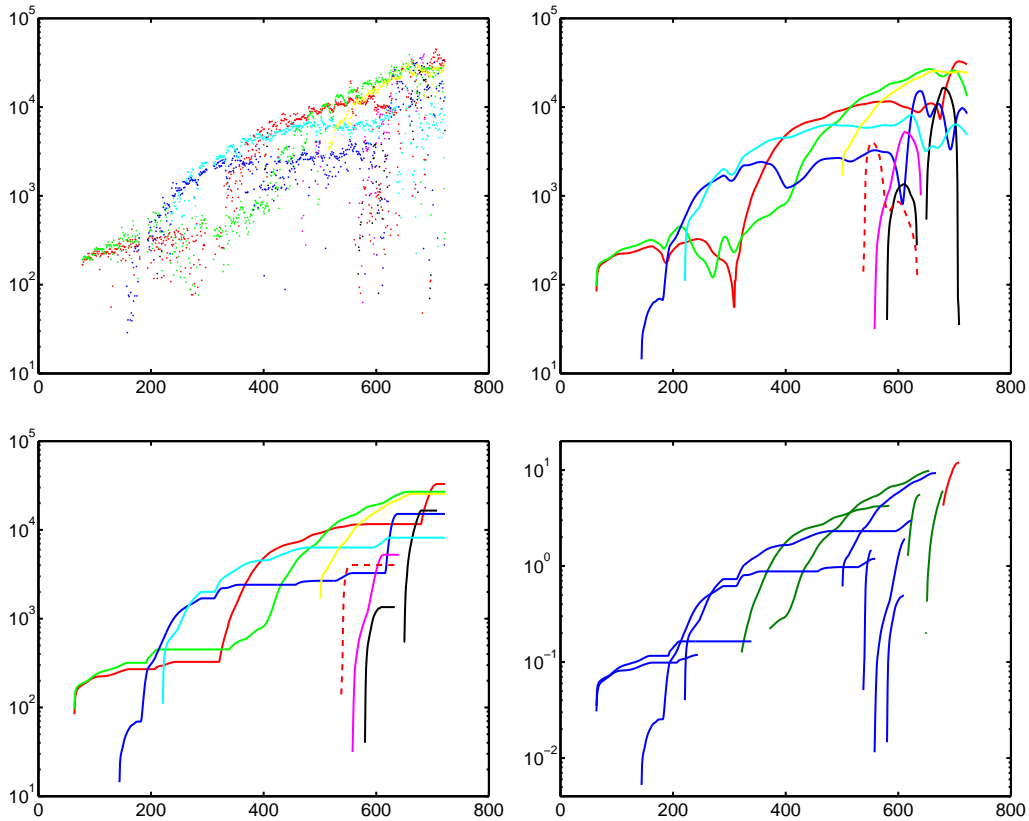


Figure 8: Measured leaf size versus time for Plant ID 79336. Top left: raw data. Different colors indicate different growth curves. Same is true for the next 2 plots. Top right: smoothed by median filter and gaps closed by normalized convolution. Bottom left: filtered to ensure monotonic increase. Bottom right: Growth curves split into curves belonging to a single leaf, horizontal beginnings and ends removed. Blue indicates the first section of a growth curve, green the second and red the third section stemming from one initial growth curve. The vertical and horizontal axes represent leaf size (cm^2) and time (hours).

298 left, e.g. red and green lines, with the corresponding lines in Figure 8 bottom right). At
 299 each curve, initial or trailing horizontal parts are removed, as they do not reliably reflect
 300 measurements, but extrapolations, only.

301 Due to the curve cutting process, the natural emergence order, i.e. that growth curve n
 302 belongs to leaf n , is no longer given. Ideally curves should be sorted by the times when
 303 leaves have a certain, predefined size. This is not possible here, as some curves start at

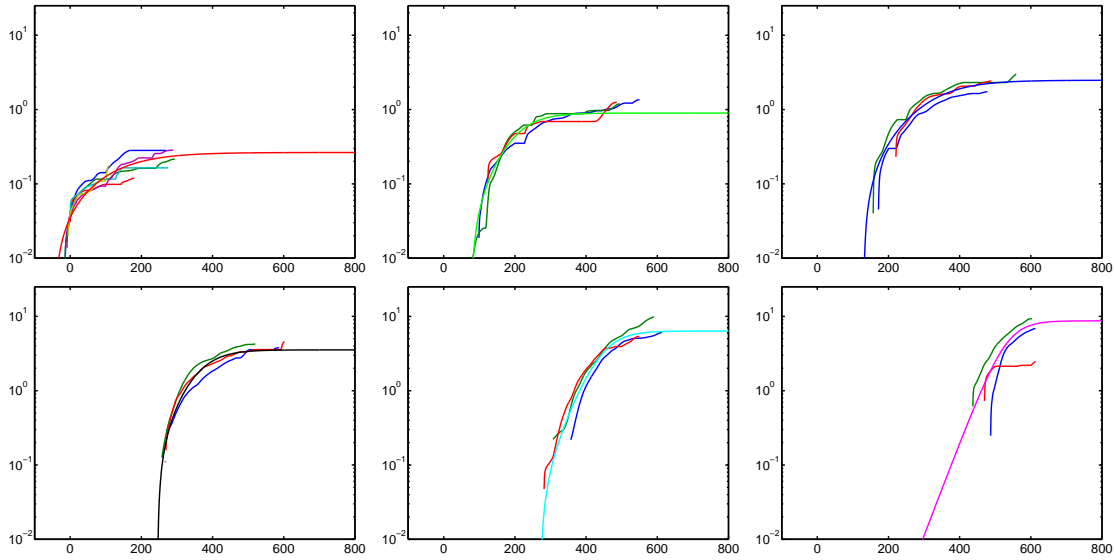


Figure 9: Mean growth curves for the treatment with more nutrients and less water (treatment 2): Single leaf growth curves of all 3 plants sorted by time of emergence, i.e. leaf number. Thick curves are the measured data, fine curve is the autocatalytic model with constant y-offset robustly fitted to all curves simultaneously. Left to right and top to bottom: cotyledons (i.e. leaf 1 and 2, being 6 curves for 3 plants), leaf 3 to 7. Cotyledons are temporally aligned such that size 0.04cm^2 corresponds to time 0h. The vertical and horizontal axes represent leaf size (cm^2) and time (hours).

304 quite large leaf sizes. As sorting by emergence time of the curves would lead to wrong
 305 ordering, we compensate the later emergence of a growth curve by fitting a tangent in log-
 306 scale (i.e. a purely exponential growth curve) to each curve and order by their time offsets.
 307 We use a high growth rate of $10\%/h$ for the tangent, being adequate due to a measurement
 308 offset (cmp. Section 3.9). The resulting growth curves sorted per leaf number of plants
 309 from the treatment with more nutrients and less water are depicted in Figure 9. There
 310 curves are temporally aligned such that the time point when the first Cotyledon reaches
 311 size 0.04cm^2 corresponds to time 0h.

312 *3.9. Leaf growth modeling*

313 To each of the leaf-number-wise sorted growth curve groups (cmp. Figure 9) a growth
314 model is fitted in a robust way (thin lines in the plots). We use the well known autocatalytic
315 growth model (see e.g. Richards (1959)) with a slight modification

$$A(t) = A_{\infty}(1 + \exp(-gr(t - \tau)))^{-1} - A_{offset} \quad , \quad (9)$$

316 where $A(t)$ is the leaf size at time t , A_{∞} is the final leaf size, gr is the growth rate, τ is
317 a time offset. A_{offset} is an offset compensating an apparent slight underestimation of the
318 true leaf size.

319 This model is fitted to the data using a robust error norm able to ignore outliers at
320 a constant high cost. We use a variant of the truncated quadratic (Blake and Zisserman
321 (1987)) where the constant cost after truncation is 10 times higher than the cost at the
322 truncation limit. By this we ensure to have a maximum amount of inliers as e.g. required
323 as optimality condition in random sample consensus (RANSAC, see Fischler and Bolles
324 (1981)).

325 The time offset τ models the leveling off of the growth curve and is not suitable to
326 estimate leaf emergence. Following Tsai et al. (1997) we use the time point t_c when a leaf
327 reaches a small given size $A(t_c) = c$. For our autocatalytic model we derive

$$t_c = \tau - \frac{1}{gr} \log \left(\frac{A_{\infty}}{c + A_{offset}} - 1 \right) \quad . \quad (10)$$

328

329 4. Results

330 4.1. Fitted leaf growth models

331 As we are here dealing with a system to measure early plant growth, we have investi-
332 gated and modeled only the first few leaves (counting cotyledons as leaves 1 and 2). When
333 plants are getting bigger, we observe large and rapid variations in the size estimates for
334 some leaves. This is because wrong segment and depth estimations occur more often dur-
335 ing this phase. Thus measurements become less reliable making leaf sorting ambiguous.
336 In Figure 10 we therefore show results for the first 7 leaves, only. Looking at fitted final
337 leaf size A_∞ for the averaged plant models we observe, that plants under Treatment 1 (see
338 Section 2) grow much larger leaves than under Treatment 2. However, not only growth
339 rates gr are higher, but also the time span $\tau - t_c$ between leaf “emergence” t_c and leveling
340 off time τ . For Treatment 1 the average growth duration is 114h, for Treatment 2 it is 99h.

341 The estimated phyllochron, i.e. the time between leaf “emergence” time points t_c ,
342 varies also slightly, average 65h for Treatment 1 and 61h for Treatment 2. Leaf 3, the
343 first leaf after the cotyledons, emerges after 2 to 3 days after these. Leaf 4 then emerges
344 quicker (1.5 to 2 days) and leaf 5 then takes 5 to 6 more days to emerge. Leaves 6 and 7
345 then again emerge quicker after 2 to 3 days. Thus for our small dataset we observe that
346 there is no constant time interval between emergence of leaves, but leaf 5 emerges with a
347 considerable delay for both treatments.

348 4.2. Benchmarking the method

349 The functioning of the framework presented in this paper strongly depends on the
350 segmentation process (step 2 of the procedure). The correct perception of plant leaves

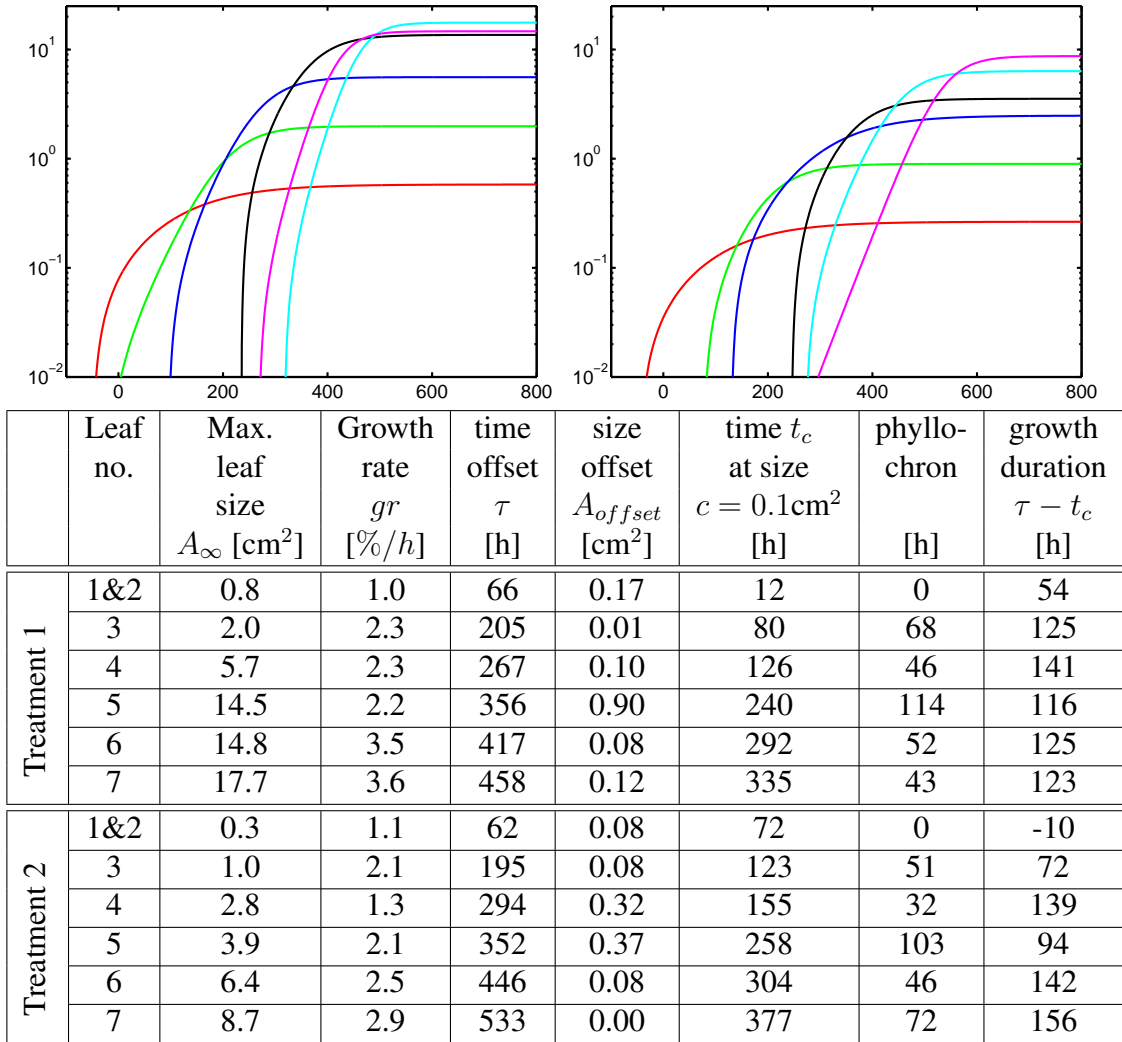


Figure 10: Fitted growth curves and parameters of autocatalytic model with constant offset A_{offset} for all leaves. Left plot: Treatment 1. Right plot: Treatment 2. The vertical and horizontal axes represent leaf size (cm^2) and time (hours).

351 represents the most critical component of the procedure. In our framework, the superpara-
352 magnetic clustering of data has been chosen for the over-segmentation of leaves due to
353 the following two reasons. First, this method accelerated on the GPU has a very high time
354 performance and processes about 10 frames per second for image sizes of 640×512 pixels.

355 Second, segments can be better merged by this algorithm using the convex hull approxi-
356 mation as compared to segments produced by conventional segmentation techniques such
357 as the graph-based or mean shift technique from Felzenszwalb and Huttenlocher (2004);
358 Comaniciu et al. (2002). This is because both of the latter techniques are dense, i.e, seg-
359 ments are forced to grow until all segments are larger than a minimum segment size. As a
360 consequence, segments often grow into the small cavities that exist in the space between
361 other segments, distorting the actual shape of segment, or can get more easily merged with
362 other segments, as can be seen in the comparative Figure 11, where corrected segments
363 for plant number 79339 using the graph-based segmentation (both middle columns) and
364 superparamagnetic clustering of data (right column) within our framework are shown for
365 selected frames.

366 In the graph-based approach the number of output segments is controlled by the thresh-
367 old k which should be lower than the recommended value ($k = 500$) to achieve the
368 over-segmentation mode. We determined experimentally that $k = 150$ guarantees over-
369 segmentation for the majority of input frames (see the middle left column), while larger k
370 values can produce dramatic merges (see the middle right column). Overall, we obtained
371 better results with the superparamagnetic clustering as compared to the graph-based tech-
372 nique.

373 We further analyzed how much the estimated number of leaves deviate from the ground
374 truth provided, and compare the performance of the superparamagnetic clustering method
375 with the one of the graph-based method Felzenszwalb and Huttenlocher (2004) when used
376 inside our framework.

377 Figure 12 shows the comparison of the estimated number of leaves for three different

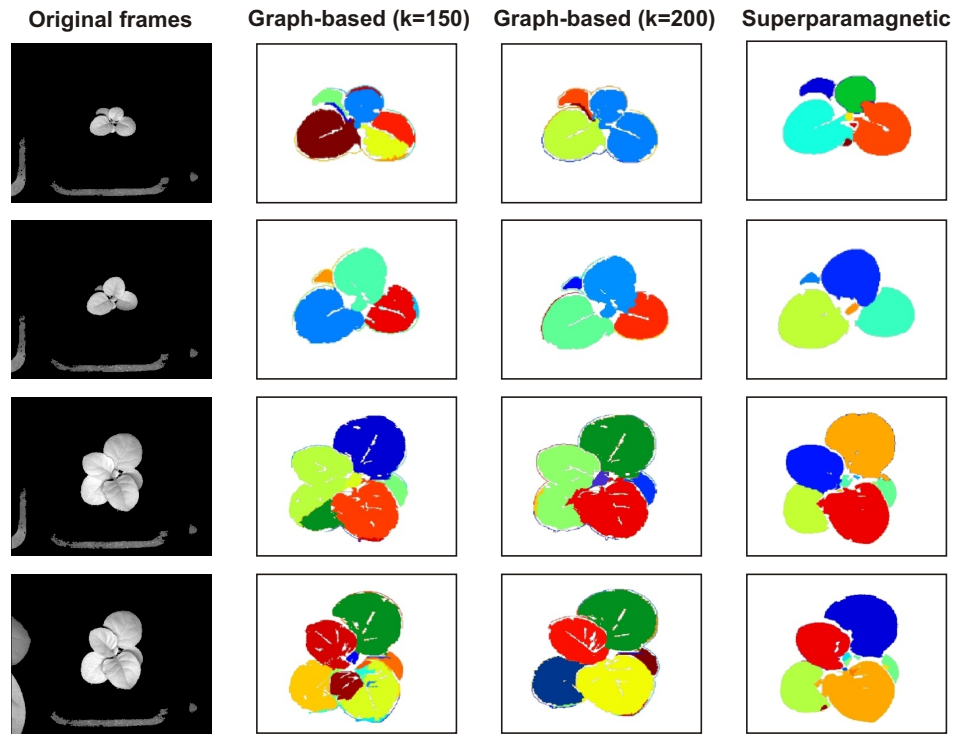


Figure 11: Leaf segmentation results obtained using the graph-based approach and the superparamagnetic clustering of data. Left column shows input near infrared (NIR) images for plant number 79339. Middle left and right columns show final segments for the graph-based method with threshold values $k = 150$ and $k = 200$, respectively. Segments from the superparamagnetic clustering are shown in the right column. Note that segments are here scaled up for a better visibility.

378 tobacco plants in the case of using the superparamagnetic clustering of data and the graph-
379 based technique with the ground-truth data. The ground-truth data is obtained through
380 human visual inspection, counting the number of leaves, including partially occluded ones.
381 Both ground truth and the automatically computed number of leaves using our framework
382 are shown for both segmentation approaches as a function of days. We can see that the
383 number of leaves estimated with the superparamagnetic clustering agrees better with the
384 ground truth than the graph-based method. However, both methods cannot handle the
385 plant number 79336 after 25 days (see the high deviation between the estimated and actual

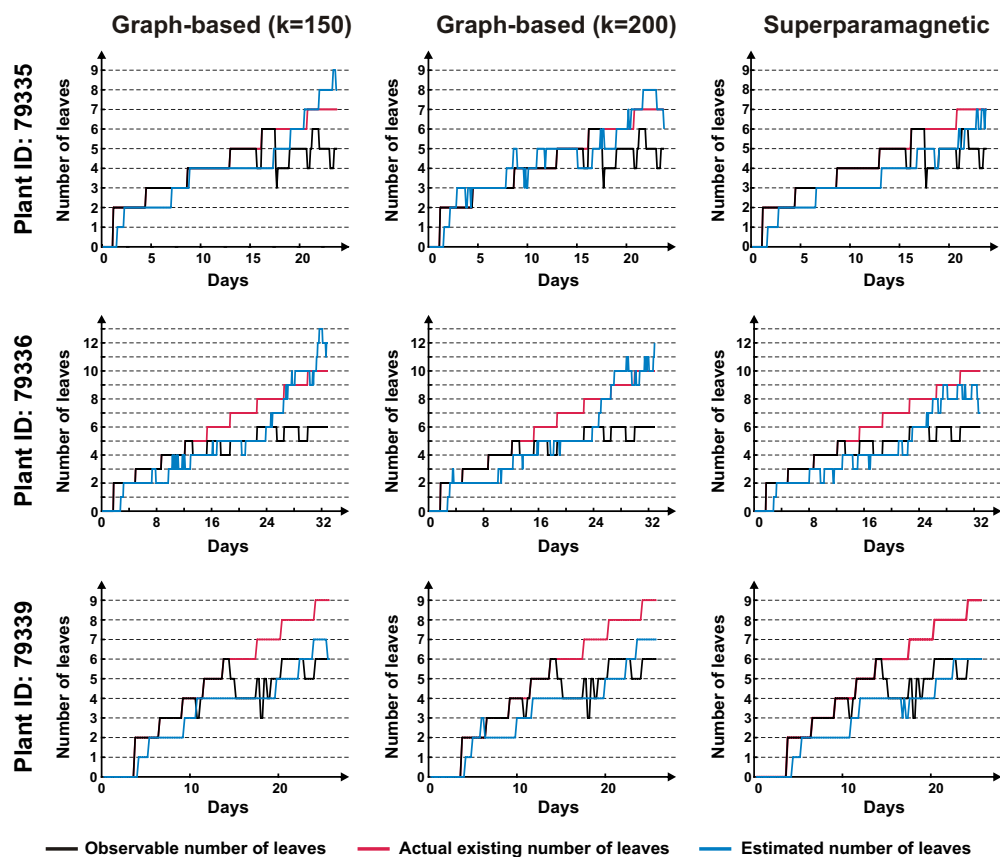


Figure 12: Comparison of the estimated number of leaves obtained for plant numbers 79335 (top row), 79336 (middle row), and 79339 (last row) using the graph-based approach and the superparamagnetic clustering of data for over-segmentation. The manually measured observable and actual existing number of leaves are used here as ground-truth data.

Plant number	Graph-based ($k = 150$)	Graph-based ($k = 200$)	Superparamagnetic
79335	1.2230	1.3519	1.0021
79336	2.0962	2.2180	1.4913
79339	0.9883	0.9022	1.0268

Table 1: The root-mean-square (RMS) error between the estimated and actual observed number of leaves for three different plants for the graph-based approach and the superparamagnetic clustering of data when used in our framework.

386 observed number of leaves in Figure 12 (middle row). A quantitative evaluation of both
387 methods with respect to the observable number of leaves based on the root-mean-square
388 error is presented in Table 1.

389 **5. Discussion**

390 The found average growth models are well in accordance with established literature.

391 Average per leaf growth rates of 2.5% (Treatment 1) or 2.0% (Treatment 2) are in the
392 same range as the growth rates found in Walter and Schurr (1999). There, in Figure 1D,
393 total leaf growth rates RGR between 12 and 18%/d, i.e. 0.5 and 0.75%/h, are reported
394 together with the observation, that the biggest leaf contributes approx. 35% of the overall
395 size and about 30 to 40% of the growth (Fig. 4B). As non-growing leaves are also taken
396 into account for total leaf growth, growth rates for growing leaves need to be significantly
397 higher than the averaging total, well in accordance with our findings.

398 Systematic increase of final leaf size A_{∞} of the first few leaves, as found for both
399 treatments, are also reported in (Tsai et al., 1997, Figure 1). Absolute sizes are obviously
400 treatment dependent, see Walter and Schurr (1999).

401 Phyllochron values reported in (Tsai et al., 1997, Figure 5, page 911) show a similar
402 behavior as our findings. Leaf 4 emerges earlier than expected and leaf 5 somewhat later.
403 The absolute duration between leaf emergence of the first 6 leaves lies however higher
404 than under our treatments, i.e. between 72h and 144h with an average of approx. 110h
405 for a treatment with $300\mu\text{E m}^{-2}\text{s}^{-1}$ photons and daily watering. Our treatments feature
406 much higher light intensities and different watering strategies. Phyllochrons found here
407 lie between 32h and 114h with averages of approx. 61h or 65h, respectively. According

408 to Munns (2002) leaf emergence rate is reduced under drought stress, thus clearly reacts
409 to environmental conditions and thus differences found may be related to treatment differ-
410 ences.

411 The framework has been successfully applied inside a robot perception-action loop
412 during experiments that were performed in the context of the EU project GARNICS. In
413 these experiments, the robot had to make decisions about plant treatment based on sen-
414 sory input, which was being processed with our multi-level pipeline, and water the plants
415 accordingly. In the final experiments of the project the robot succeeded in taking care of
416 the plants over a period of about three weeks, where the treatment found by the system
417 resulted in a generally higher growth rate than in any of the training data.

418 **6. Conclusion**

419 We presented a novel multi-level procedure for finding and tracking of leaves of grow-
420 ing tobacco plants which allowed us to measure automatically important plant parameters,
421 i.e., number of leaves and leaf size, as a function of time. The main challenge originates
422 from the complex appearance of plants, making it difficult to segment plant organs. We
423 used leaf-shape models to improve leaf segmentation and could successfully segment and
424 track tobacco-plant leaves to up to an age of about 25 days. Beyond this growth stage, leaf
425 segmentation turned out to be increasingly hard. As leaves grew older, we often observed
426 under-segmentation errors. Fig. 13 shows examples where such under-segmentation ef-
427 fects have been observed. These problems can only be resolved by further improving the
428 segmentation procedure.

429 The convex-hull approximation works well for tobacco plants but might have to be

430 augmented using more sophisticated leaf models when dealing with other types of plants.
431 The border detection as well as the depth reasoning could be improved in the future using
432 e.g. a structured-light imaging system (Geng (2011)). The accuracy of the plant models
433 estimated in Section 4.1 can further be improved by simply increasing the number of
434 observed plants. Ellipses are used to estimate the size of the leaves from the segment
435 boundaries in the last step of the algorithm. For tobacco plants, the ellipse model is an
436 appropriate choice. For other plants, another leaf-shape model could be used instead of
437 the ellipse. Assumptions about the leaf shape are also being made during the merging step
438 (see Section 3.5). It is assumed that leaves have a convex shape. In some approximation,
439 this holds for many types of plants, but it is not generally true. For non-convex leaf-shapes,
440 the merging algorithm would have to be modified, and a specific leaf model could be fitted
441 to the boundary of the object instead of finding its convex hull. Furthermore, we are
442 currently analyzing plant vein structures which can then be used to correct segments and
443 fit more accurate ellipses. Initial steps given in Johansson (2010) show promising results
444 along this line.



Figure 13: Under-segmentation errors observed once leaves are getting bigger. Merged segments have the same color.

445 **Acknowledgements**

446 We thank Torge Herber from Forschungszentrum Jülich for the image acquisition.
447 The research leading to these results has received funding from the European Commu-
448 nity's Seventh Framework Programme FP7/2007-2013 - Challenge 2 - Cognitive Systems,
449 Interaction, Robotics - under grant agreement No 247947 - GARNICS. Babette Dellen
450 acknowledges support from the Spanish Ministry for Science and Innovation through a
451 Ramon y Cajal program.

452 **References**

- 453 A. Abramov, Pauwels K., J. Papon, F. Wörgötter, and B. Dellen. Real-time segmentation
454 of stereo videos on a portable system with a mobile gpu. *IEEE Transactions on Circuits
455 and Systems for Video Technology*, 9(22):1292–1305, 2012.
- 456 Guillem Alenyà , Babette Dellen, Sergi Foix, and Carme Torras. Robotized plant probing:
457 Leaf segmentation utilizing time-of-flight data. *IEEE Robot. Automat. Mag.*, 20(3):50–
458 59, 2013.
- 459 G. Alenyà, B. Dellen, and C. Torras. 3d modelling of leaves from color and tof data for
460 robotized plant measuring. *Proc. IEEE Intl. Conf. on Robotics and Automation*, 2011a.
- 461 G. Alenyà, F. Moreno-Noguer, A. Ramisa, and C. Torras. Active perception of deformable
462 objects using 3d cameras. In *Workshop de Robotica Experimental*, pages 434–440,
463 Seville, 2011b.
- 464 B. Biskup, H. Scharr, U. Schurr, and U. Rascher. A stereo imaging system for measuring

465 structural parameters of plant canopies. *Plant, Cell and Environment*, 30:1299–1308,
466 2007.

467 Andrew Blake and Andrew Zisserman. *Visual Reconstruction*. MIT Press, Cambridge,
468 MA, USA, 1987. ISBN 0-262-02271-0.

469 G. Bradski. The OpenCV Library. *Dr. Dobb's Journal of Software Tools*, 2000.

470 Chung-Fang Chien, Yu-Che Cheng, and Ta-Te Lin. Robust ellipse detection based on
471 hierarchical image pyramid and hough transform. *Journal of the Optical Society of*
472 *America*, 28(4):581–589, 2011.

473 Dorin Comaniciu, Peter Meer, and Senior Member. Mean shift: A robust approach toward
474 feature space analysis. *IEEE Transactions on Pattern Analysis and Machine Intelli-*
475 *gence*, 24:603–619, 2002.

476 CORESTA CORESTA. A scale for coding growth stages in tobacco
477 crops, Feb. 2009. URL [http://www.coresta.org/Guides/
478 Guide-No07-Growth-Stages_Feb09.pdf](http://www.coresta.org/Guides/Guide-No07-Growth-Stages_Feb09.pdf).

479 J. De Vylder, W. Philips, and D. Van Der Straeten. Multiple leaf tracking using com-
480 puter vision methods with shape constraints. In *Proc. of the International Conference*
481 *on Sensing Technologies for Biomaterial, Food, and Agriculture (SPIE: SeTBio2013)*,
482 Yokohoma, Japan, 2013.

483 Jonas De Vylder, Daniel Ochoa Donoso, Wilfried Philips, Laury Chaerle, and Dominique
484 Van Der Straeten. Leaf segmentation and tracking using probabilistic parametric active

485 contours. In A Gagalowicz and Wilfried Philips, editors, *Lecture Notes in Computer*
486 *Science*, volume 6930, pages 75–85. Springer, 2011.

487 Pedro F. Felzenszwalb and Daniel P. Huttenlocher. Efficient graph-based image segmen-
488 tation. *International Journal of Computer Vision*, 59(2):167–181, 2004.

489 Martin A. Fischler and Robert C. Bolles. Random sample consensus: A paradigm for
490 model fitting with applications to image analysis and automated cartography. *Commun.*
491 *ACM*, 24(6):381–395, June 1981. ISSN 0001-0782. doi: 10.1145/358669.358692.

492 Jason Geng. Structured-light 3d surface imaging: a tutorial. *Adv. Opt. Photon.*, 3(2):
493 128–160, Jun 2011.

494 S. L. Horowitz and T. Pavlidis. Picture Segmentation by a directed split-and-merge pro-
495 cedure. *Proceedings of the 2nd International Joint Conference on Pattern Recognition,*
496 *Copenhagen, Denmark*, pages 424–433, 1974.

497 Jian Jin and Lie Tang. Corn plant sensing using real-time stereo vision. *Journal of Field*
498 *Robotics*, 26(6-7):591–608, 2009.

499 Peter Johansson. Plant condition measurement from spectral reflectance data. Master’s
500 thesis, Linköping University, Computer Vision, 2010.

501 Watcharin Kaewapichai and Pakorn Kaewtrakulpong. Robust ellipse detection by fitting
502 randomly selected edge patches. *World Academy of Science, Engineering and Technol-*
503 *ogy*, pages 30–33, 2008.

- 504 H. Knutsson and CF. Westin. Normalized and differential convolution: Methods for inter-
505 polation and filtering of incomplete and uncertain data. In *CVPR'93*, pages 515–523,
506 New York City, USA, 1993.
- 507 B.I. Loch, J.A. Belward, and J.S.Hanan. Application of surface fitting techniques for the
508 representation of leaf surfaces. *MODSIM 2005 International Congress on Modelling
509 and Simulation*, pages 1272–1278, 2005.
- 510 T. B. Moeslund, M. Aagaard, and D. Lerche. 3d pose estimation of cactus leaves using
511 an active shape model. In *Application of Computer Vision, 2005. WACV/MOTIONS '05
512 Volume 1. Seventh IEEE Workshops on*, volume 1, pages 468–473, 2005.
- 513 R. Munns. Comparative physiology of salt and water stress. *Plant, Cell and Environment*,
514 25(2):239–250, 2002.
- 515 G. Polder, G.W.A.M. van der Heijden, H. Jalink, and J.F.H. Snel. Correcting and matching
516 time sequence images of plant leaves using penalized likelihood warping and robust
517 point matching. *Computers and Electronics in Agriculture*, 55(1):1 – 15, 2007. ISSN
518 0168-1699.
- 519 L. Quan, P. Tan, G. Zeng, L. Yuan, J. Wang, and S.B. Kang. Image-based plant modelling.
520 *ACM Siggraph*, pages 599–604, 2006.
- 521 F. J. Richards. A flexible growth function for empirical use. *Journal of Experimental
522 Botany*, 10(2):290–301, June 1959. doi: 10.1093/jxb/10.2.290.
- 523 L.O.L.A. Silva, M.L. Koga, C.E. Cugnasca, and A.H.R. Costa. Comparative assess-

524 ment of feature selection and classification techniques for visual inspection of pot plant
525 seedlings. *Computers and Electronics in Agriculture*, 97(0):47 – 55, 2013.

526 Ge Song and Hong Wang. A fast and robust ellipse detection algorithm based on pseudo-
527 random sample consensus. In *Proceedings of the 12th International Conference on*
528 *Computer Analysis of Images and Patterns*, pages 669–676, 2007.

529 Y. Song, R. Wilson, R. Edmondson, and N. Parsons. Surface modelling of plants from
530 stereo images. *6th IEEE Intl. Conf. on 3D Digital Imaging and Modelling*, 2007.

531 Ch.-H. Teng, Y.-T. Kuo, , and Y.-S. Chen. Leaf segmentation, classification, and three-
532 dimensional recovery from a few images with close viewpoints. *Optical Engineering*,
533 50(3), 2011. doi: 10.1117/1.3549927.

534 C. H. Tsai, A. Miller, M. Spalding, and S. Rodermel. Source strength regulates an early
535 phase transition of tobacco shoot morphogenesis. *Plant Physiol*, 115(3):907–914, 1997.

536 Marcus Wallenberg, Michael Felsberg, Per-Erik Forssén, and Babette Dellen. Leaf seg-
537 mentation using the kinect. In *Proceedings of SSBA 2011 Symposium on Image Analysis*,
538 2011.

539 A. Walter and U. Schurr. The modular character of growth in nicotiana tabacum plants un-
540 der steady-state nutrition. *Journal of Experimental Botany*, 50(336):1169–1177, 1999.
541 doi: 10.1093/jxb/50.336.1169.

542 Jianlun Wang, Jianlei He, Yu Han, Changqi Ouyang, and Daoliang Li. An adaptive thresh-
543 olding algorithm of field leaf image. *Computers and Electronics in Agriculture*, 96(0):
544 23 – 39, 2013. ISSN 0168-1699.

545 F. Wörgötter, A. Abramov, E. E. Aksoy, and B. Dellen. Method and device for estimating
546 development parameters of plants. *Patent office WO, Patent number 2013083146*, 2013.